

Effects of Strain Rates on Mechanical Properties and Fracture Mechanism of DP780 Dual Phase Steel

Shengci Li, Yonglin Kang, Guoming Zhu, and Shuang Kuang

(Submitted October 10, 2014; in revised form February 12, 2015; published online April 3, 2015)

The mechanical properties of DP780 dual phase steel were measured by quasi-static and high-speed tensile tests at strain rates between 0.001 and 1000 s⁻¹ at room temperature. The deformation and fracture mechanisms were analyzed by observation of the tensile fracture and microstructure near the fracture. Dynamic factor and feret ratio quantitative methods were applied to study the effect of strain rate on the microstructure and properties of DP780 steel. The constitutive relation was described by a modified Johnson-Cook and Zerilli-Armstrong model. The results showed that the strain rate sensitivity of yield strength is bigger than that of ultimate tensile strength; as strain rate increased, the formation of microcracks and voids at the ferrite/martensite interface can be alleviated; the strain rate effect is unevenly distributed in the plastic deformation region. Moreover, both models can effectively describe the experimental results, while the modified Zerilli-Armstrong model is more accurate because the strain-hardening rate of this model is independent of strain rate.

Keywords deformation, dual phase steel, fracture, mechanical properties

1. Introduction

Dual phase steel (DP) has a broad application prospect in vehicles due to its combination of high strength, good ductility, high initial work-hardening rates, low yield-to-tensile ratio, and continuous yielding (Ref 1). The strain rate achieves 1000 s⁻¹ in a typical real auto-body crash (Ref 2), while the mechanical properties and deformation behavior of materials are significantly different between dynamic loading conditions and quasi-static conditions (Ref 3, 4). Therefore, it is necessary to study the effects of strain rates on mechanical properties and fracture mechanism of DP steels for the safety of automobiles.

Oliver et al. (Ref 5, 6) studied the microstructural changes through dynamic tensile testing of DP steels at low and high strain rates; the full crash performance data from the dynamic tensile tests and crushing of box sections were also obtained. Huh et al. (Ref 7) found that pre-strain affects the yield stress and the ultimate tensile strength of DP600 steels at strain rates over 1 s⁻¹. The tensile properties and deformation behavior of DP780 were also studied by SEM, TEM, and Split Hopkinson Tensile Bar testing (SHTB) (Ref 8, 9). Moreover, many optimized constitutive models were established (Ref 10, 11).

Yonglin Kang, School of Materials Science and Engineering, University of Science and Technology Beijing, Beijing 100083, China; and State Key Laboratory for Advanced Metals and Materials, University of Science and Technology Beijing, Beijing 100083, China; and **Shengci Li** and **Guoming Zhu**, School of Materials Science and Engineering, University of Science and Technology Beijing, Beijing 100083, China; and **Shuang Kuang**, Technical Research Institute, Shougang Corporation, Ltd., Beijing 100043, China. Contact e-mails: lishengci1988@163.com and kangylin@ustb.edu.cn.

Although the microstructure and properties of DP steels have been studied by many researchers, the dynamic deformation behavior is still at the exploration stage, especially for high strength DP780 dual phase steel. Besides, few researchers analyzed the fracture mechanism of DP steel by quantitative methods.

In the present study, the dynamic tensile properties of DP780 cold-rolled dual phase steel were obtained by a high-speed tensile testing machine. The deformation and fracture mechanisms were analyzed quantitatively, and the constitutive equation was described by two models. The results provide a reference for this product in the practical application.

2. Experimental Procedure

The materials investigated in this study were 1.2-mm-thick industrial production of ferrite-martensite cold-rolled dual phase steel sheets with excellent flatness. The chemical composition is given in Table 1.

The samples for tensile tests were machined by wire cut electrical discharge machining. Figure 1(a) shows the specimen dimension for lower strain rates, and Fig. 1(b) was for higher strain rates. The specimen length direction was parallel to the rolling direction. The tests were performed with a WDW-200D computer-controlled electronic universal testing machine at strain rates from 10⁻³ to 0.067 s⁻¹; for the high strain rates (1, 10, 100, 500, 1000 s⁻¹), the tests were conducted on a ZWICK HTM5020 high-speed tensile testing machine. The stress data were acquired by hellogh dynamic strain indicator with a sampling rate of 20 Msps. A strain gage and strain force transducer were pasted on the samples, the data acquisition system obtained the signal output by the hellogh dynamic strain indicator, and the relationship between the signal and stress was standardized, so the stress data could be obtained. The strain was measured by a digital image correlation system, Vic-2D. A Photron SA1.1 high-speed camera was used to record the whole drawing process. The high-speed tensile testing machine with a

servohydraulic control system can achieve 0-20 m/s constant loading speed, and the maximum load reaches 50 kN.

Figure 2 shows the macroscopic morphology of the samples after tensile testing at different strain rates; most of the fractures were perpendicular to the tensile axis, but samples at strain rate of 0.067, 500, and 1000 s^{-1} fracture in a direction nearly 45° to the tensile axis. Figure 3 shows the tensile process at strain rates of 1 s^{-1} recorded by the high-speed camera. As shown in Fig. 3(b), the sample necked slightly after a certain deformation, the deformation zone became more tenuous, and the color of the black spots on the sample faded; with the test continuing, cracks can be observed in the necking area, as the white arrow shown in Fig. 3(c); the cracks continued to expand until the final fracture occurred.

After all the tensile tests were finished, specimens were machined by wire cut electrical discharge machining. The fracture morphology was captured by SEM after ultrasonic cleaning. Surface morphology near the fracture was observed

Table 1 Chemical composition of the investigated steel (wt.%)

C	Si	Mn	P	S	Cr	Al	Nb
0.15	0.50	1.71	0.010	0.003	0.31	0.018	0.01

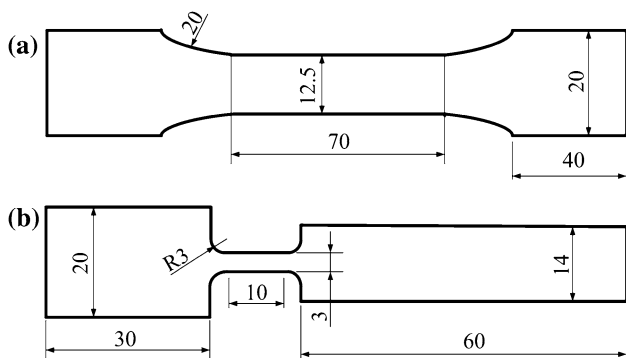


Fig. 1 Tensile specimen geometry for (a) low strain rates and (b) high strain rates (in mm)

by optical microscopy (OM) and SEM after grinding, polishing, and etching with 4% nital solution.

3. Results and Discussion

3.1 Microstructure

The microstructure of the as-received DP780 steel is ferrite and martensite as shown in Fig. 4. The typical dual phase microstructure was obtained by annealing treatment on the ferrite + pearlite cold-rolled sheet in the continuous annealing line. The annealing process comprised austenitizing at 800-820 °C, cooling slowly to 680-700 °C followed by quenching to 460 ± 5 °C; the strip velocity was 90-120 m/min. The diffusion rate of manganese in ferrite is much higher than in austenite, making the formation of a manganese-rich rim (Ref 12). As a result, the hardenability of the edge portion is higher than the central portion for austenite islands, producing a martensite rim in the edge after quenching. Energy-dispersive spectrometer (EDS) results show that the carbon content in martensite was about 0.32 wt.%. ImageJ2× calculation results indicated that the volume fraction of martensite is was about 49%, the average ferrite grain size was 3.9 μm .

3.2 Mechanical Properties

Figure 5 shows the engineering stress-strain curves of the investigated steel at different strain rates. In the elastic deformation stage, the elastic modulus of DP780 steel had no significant change. It is known that all dynamic test techniques are unavoidably inaccurate in the low deformation region, including the elastic region. In addition to the fact that it takes time to come to a stable clamp velocity of the machine and to come to a stable strain rate in the sample, it also takes time to establish a state of quasi-static equilibrium in the sample. If that equilibrium state is not yet reached, the test data are not representative for the tested material. So, it is not proper to conclude that strain rate has no significant influence on the elastic deformation stage of DP780 steel. However, the plastic deformation was notably affected by strain rate.

Figure 6 shows the effect of strain rate on the yield strength (YS) and ultimate tensile strength (UTS) of DP780 steel. At low strain rates (0.001-0.067 s^{-1}) condition, the YS and UTS

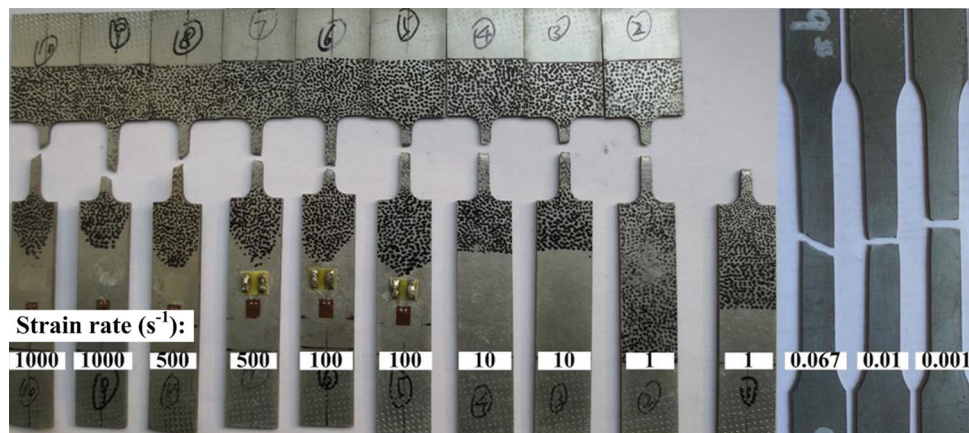


Fig. 2 The macroscopic morphology of the samples after tensile tests at different strain rates

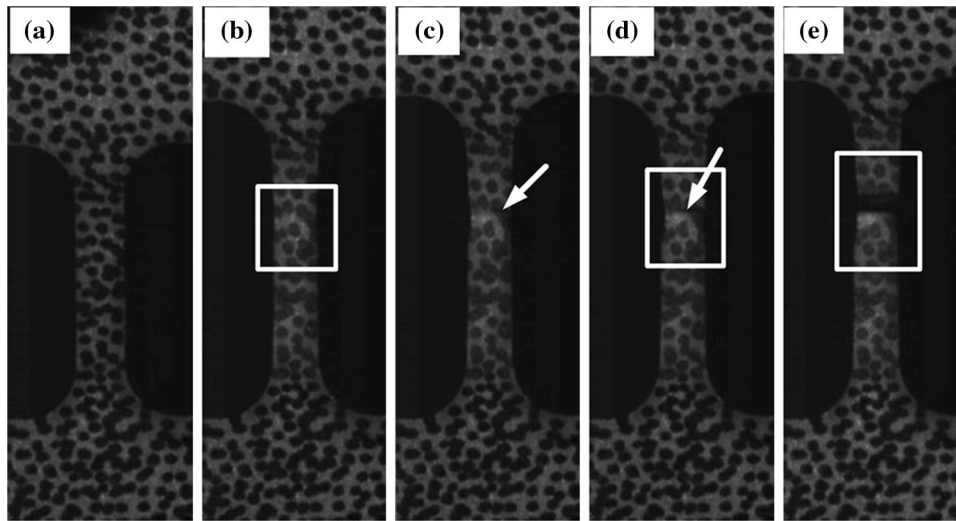


Fig. 3 Tensile process at strain rates of 1 s^{-1} recorded by high-speed camera: (a) initial state; (b) slight necked; (c) cracks appeared; (d) cracks continued to expand; and (e) final fracture

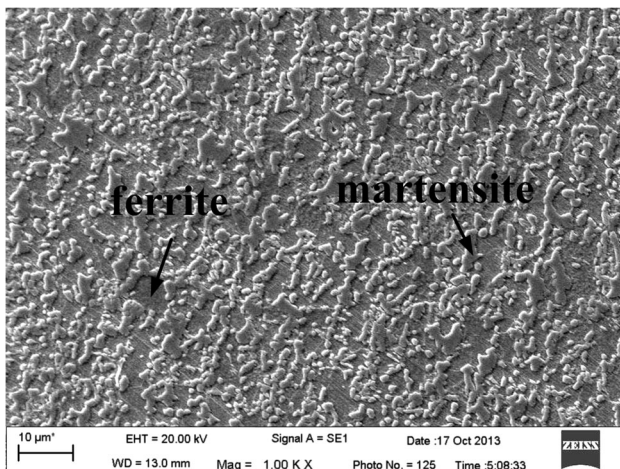


Fig. 4 SEM micrographs of the as-received DP780 steel

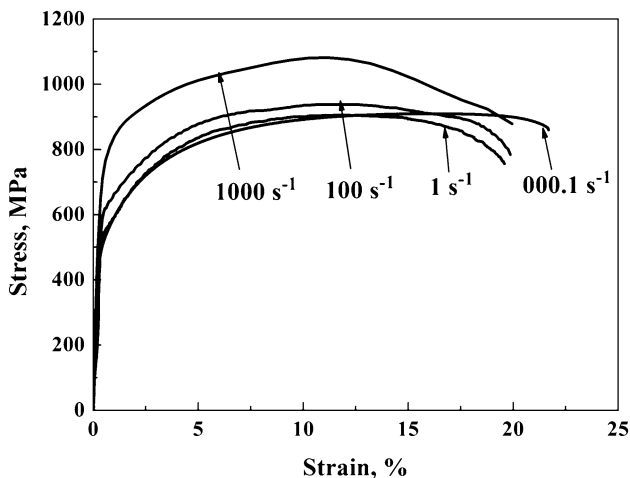


Fig. 5 Engineering stress-strain curves of the investigated steel at different strain rates

changed very little with increasing strain rates, which indicates that the strength of the investigated steel is insensitive to the variation of strain rates. After the strain rate reached 1 s^{-1} , the loading speed became so fast that the rotation of the crystal surface along the loading force was not sufficient, the growth and extension of slip was blocked. As a result, the initial plastic deformation resistance, i.e., the yield strength, increased with strain rate. In addition, the generation of strain hardening will hinder the development of deformation, which also increased the yield stress. At strain rates of $1\text{-}500 \text{ s}^{-1}$, tensile strength increased only about 50 MPa, but it dramatically increased to 1103 MPa at 1000 s^{-1} . When the strain rate increased to 1000 s^{-1} , the degree of dislocation tangles became so severe that the work-softening effect caused by the adiabatic temperature rise and the coordinating role of multisystem slips could not offset the increase of dislocation motion resistance; as a result, the UTS increased rapidly.

Generally, the strain rate sensitivity of dual phase steel can be evaluated by the dynamic factor (Ref 13), which refers to the ratio of strength under high strain rate and low strain rate. In this study, the strength at a strain rate of 0.001 s^{-1} was defined as divisor to calculate the dynamic factors of YS and UTS, as shown in Fig. 7. As it can be seen, both dynamic factor of YS and dynamic factor of UTS increased with an increase in strain rate, embodying the effect of strain rate hardening on dynamic deformation behavior of dual phase steel. However, the dynamic factors of YS were larger than the dynamic factors of UTS, which means the strain rate sensitivity of yield strength is bigger than that of ultimate tensile strength.

In Fig. 8, the uniform elongation and post-uniform elongation corrected by Barba's law were discussed. As can be seen, the uniform elongation decreased with strain rate at low strain rate ($0.001\text{-}0.067 \text{ s}^{-1}$) conditions. When the strain rate increased to 1 s^{-1} , the uniform elongation reduced to 11.2%, and basically kept unchanged as the strain rate increased. The elongation at higher strain rate was stabilized at a certain level by comprehensive function of two mechanisms: on one hand, there is not enough time for dislocations to move, resulting in the decrease of plasticity; on the other hand, the work-softening effect caused by the adiabatic temperature rise (Ref 14) will increase the plasticity. The post-uniform elongation is also presented in Fig. 8. As can

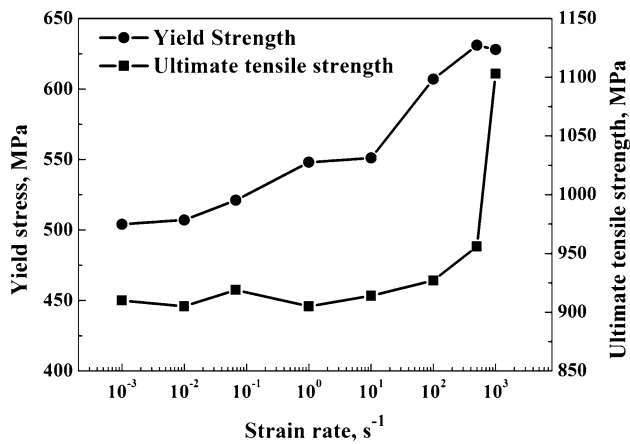


Fig. 6 Effect of strain rate on the yield strength and ultimate tensile strength of DP780 steel

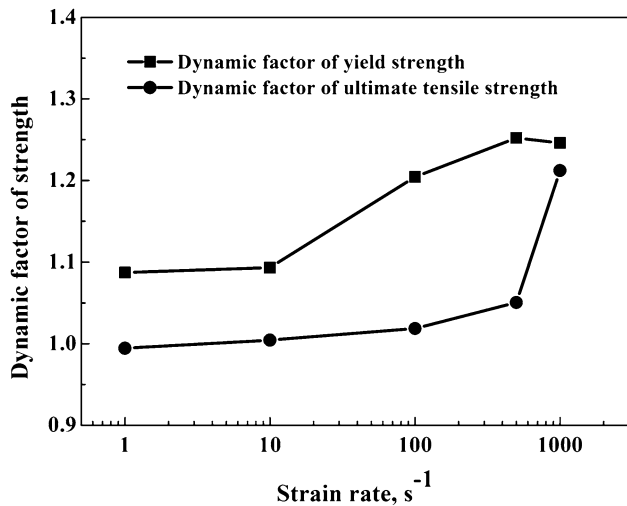


Fig. 7 Dynamic factors of the investigated DP780 steel at different strain rates

be seen, the post-uniform elongation increased with strain rate at low strain rate (0.001-0.067 s⁻¹) conditions. When the strain rate increased to 1 s⁻¹, the post-uniform elongation reduced to 2.35%, and showed a similar trend as the uniform elongation.

3.3 Fracture Mechanism

The tensile fracture morphology of DP780 steel at different strain rates is shown in Fig. 9. Many dimples which were fully formed at plastic deformation stage were observed at low strain rate (0.001-0.067 s⁻¹) conditions, and the fracture morphology did not significantly change. As the strain rate increased, the dimples became more uneven in size, the large dimples were much deeper, and the fluctuation of the fracture was more severe. Besides, an increasing number of voids can be observed due to the spalling of the hard martensite phase, since the connecting force of the ferrite/martensite interface will be weaker at higher strain rate (Ref 15).

Figure 10 shows the surface morphology near the fracture after tensile testing at different strain rates. Yellow arrows show the microcracks and voids formed at ferrite-martensite interface, and blue arrows show the cracks and voids formed by the fracture of martensite. In order to analyze the defects quantitatively, the percentage of microcracks and voids formed by different

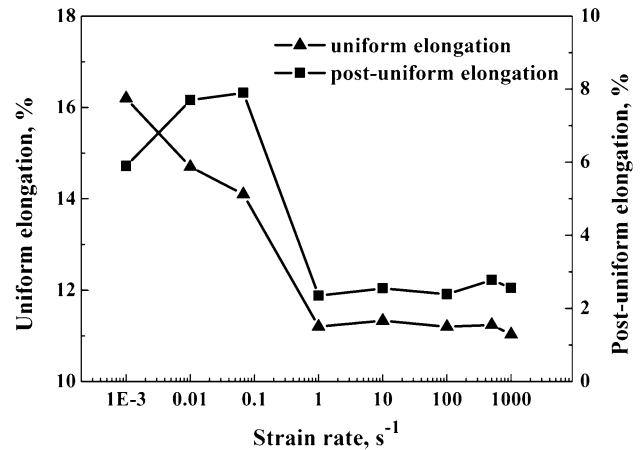


Fig. 8 Effect of strain rate on uniform elongation and the ratio of uniform elongation to post-uniform elongation

mechanism was counted, as shown in Fig. 11. Three fields were captured for each sample, and about 40 cracks and voids of each field were counted to obtain an accurate average. At low strain rates (0.001 s⁻¹), only a few microcracks and voids that formed at the ferrite/martensite interface near the fracture tip were observed. As the strain rate increased, more microcracks and voids that mainly formed at the ferrite/martensite interface were observed. More and more microcracks and voids were formed by the fracture of martensite at higher strain rate; the formation by the fracture of martensite increased with increasing in strain rate. The difference of the plastic strain energy between ferrite and ferrite/martensite interface decreased since the dislocation density and dislocation tangles significantly increased, alleviating the formation of microcracks and voids at ferrite/martensite interface (Ref 8). However, the crack formation at the ferrite/martensite interface was still the major mechanism. It is interesting to find that the first type (yellow arrows) leads to more elongated voids, whereas the second one (blue arrows) leads to more spherical voids. The martensite near the tensile fracture also deformed more significantly at higher strain rate due to the work-softening effect caused by the adiabatic temperature rise.

Feret ratio (Ref 5), which refers to the ratio of grain size along the tensile direction and perpendicular to the tensile direction, was used to describe the level of plastic deformation within the microstructure. The specimen was sectioned along the tensile direction, and then the sectioned surface was prepared to observe with an optical microscope at 2 mm intervals from the fracture tip along the tensile direction. Two fields were captured for each position, and 100 ferrite grains of each field were measured by the Imagetool software to obtain an accurate average. Figure 12 illustrates the measured Feret ratio for the investigated DP780 steels. The nonlinear decrease in average Feret ratio with increasing distance from the fracture tip indicates that the strain rate effect is not evenly distributed in the plastic deformation region. Moreover, the specimens after tensile testing showed a big difference in Feret ratio when compared to the as-received state, and the average Feret ratio at higher strain rate is larger than the corresponding Feret ratio at lower strain rate, indicating a greater degree of microstructure deformation at higher strain rate.

As can be seen in Fig. 10 and 12, the necking region plastic deformation became more significantly at higher strain rate than at lower strain rate. Figure 8 indicates that the ratio of post-

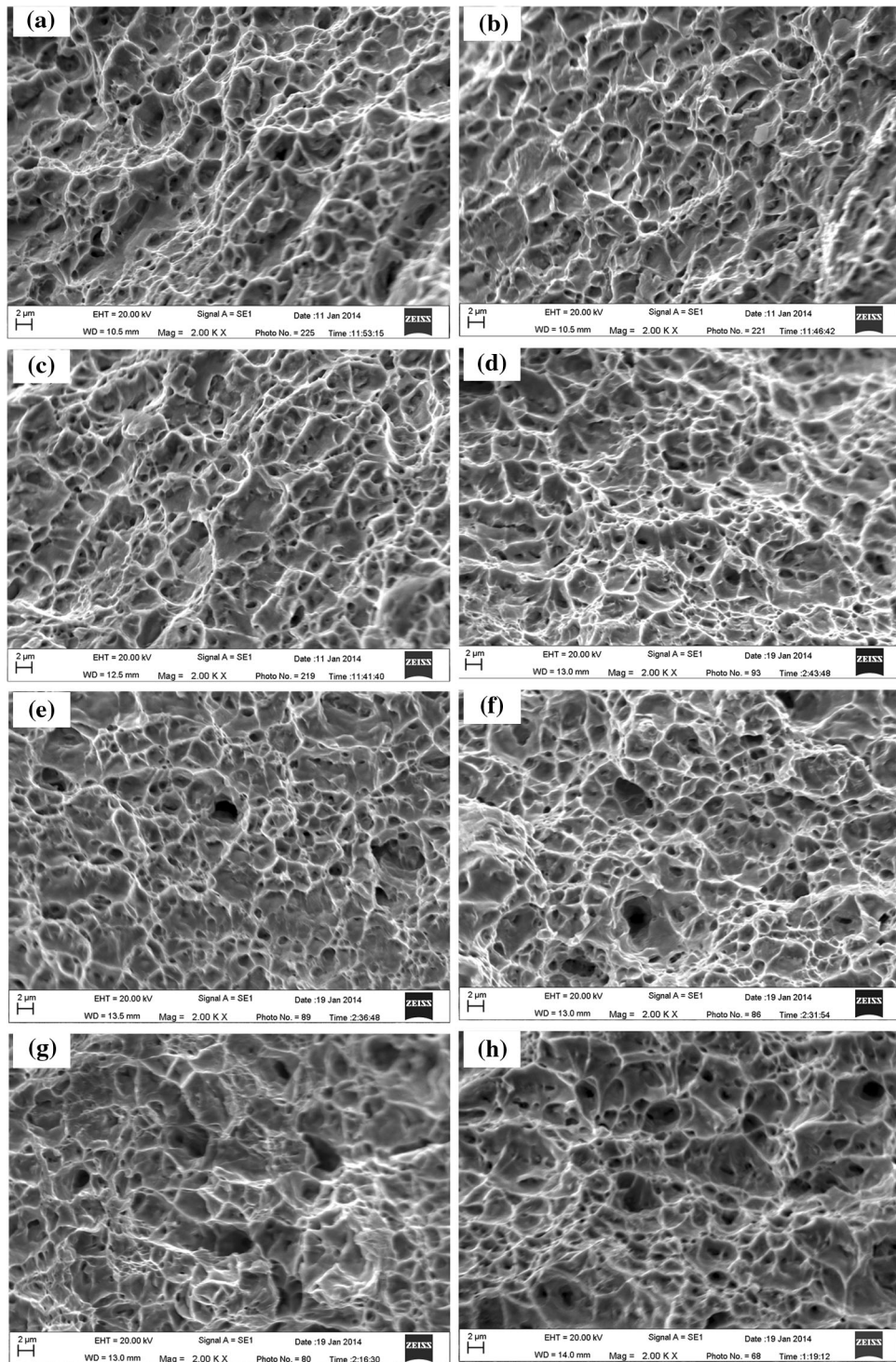


Fig. 9 Tensile fractographs of DP780 steel at strain rates of (a) 0.001/s; (b) 0.01/s; (c) 0.067/s; (d) 1/s; (e) 10/s; (f) 100/s; (g) 500/s; (h) 1000/s

uniform elongation to uniform elongation increased with strain rate. When the plastic deformation is small, only ferrite deformed, so the void and crack are easier to form at ferrite/martensite interface. However, if the plastic deformation is big enough, the concentrated stress at the ferrite/martensite interface will make the martensite deformed too, so more voids and cracks that formed by the fracture of martensite can be seen.

3.4 Constitutive Modeling

Currently, Johnson-Cook (JC) constitutive model (Ref 16) and Zerrilli-Armstrong (ZA) constitutive model (Ref 17) are commonly used because of their simplicity and accuracy. Parameters for work hardening, strain rate hardening, and thermal softening are introduced in both models. Two models were applied to describe the dynamic behavior of the inves-

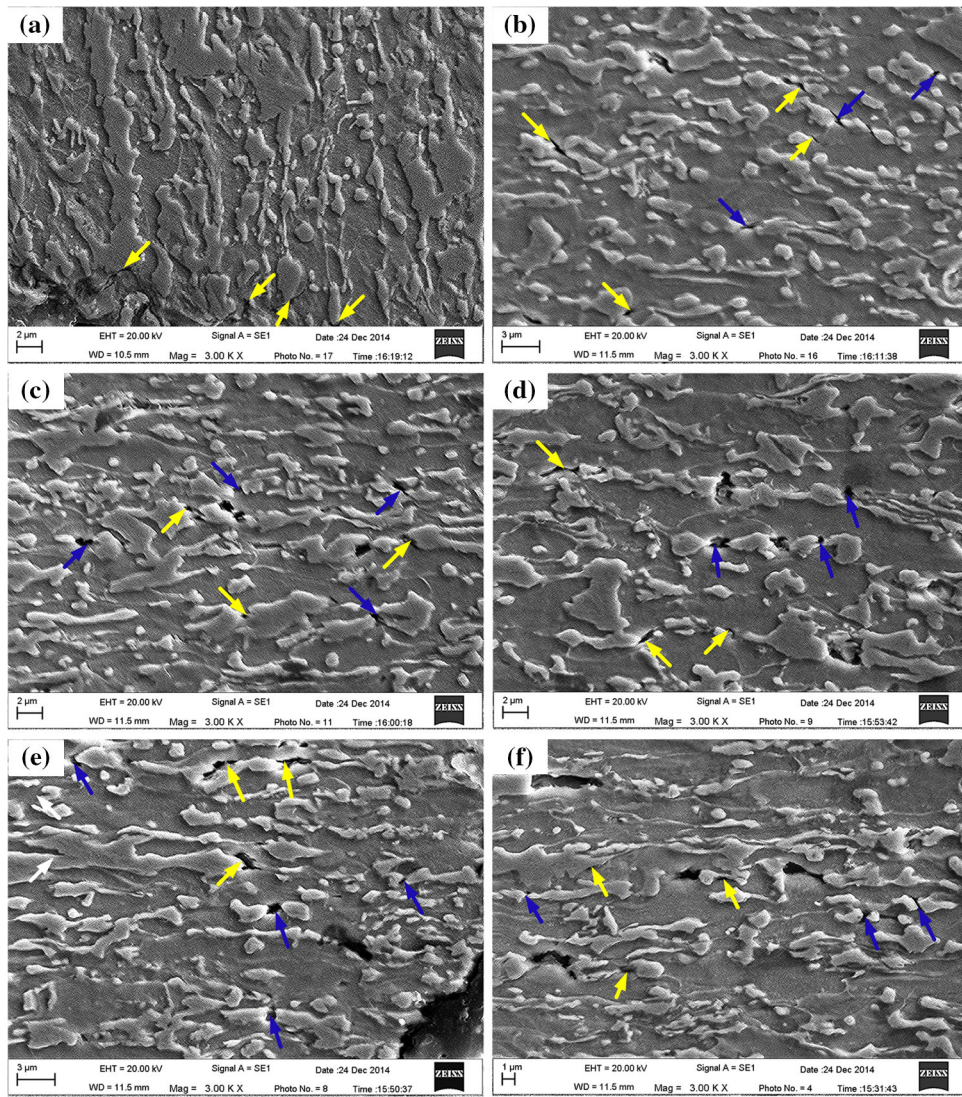


Fig. 10 Surface morphology near the fracture after tensile test at strain rates of (a) 0.001/s; (b) 1/s; (c) 10/s; (d) 100/s; (e) 500/s; (f) 1000/s. Yellow arrows show the microcracks and voids formed at ferrite-martensite interface, and blue arrows show the cracks and voids formed by the fracture of martensite

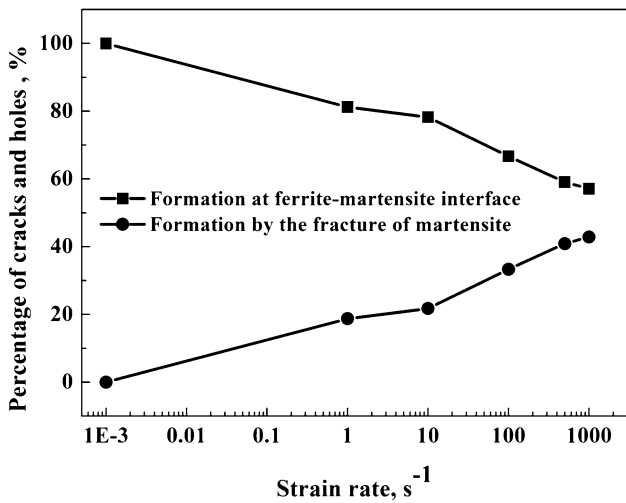


Fig. 11 The percentage of microcracks and voids formed by different mechanisms

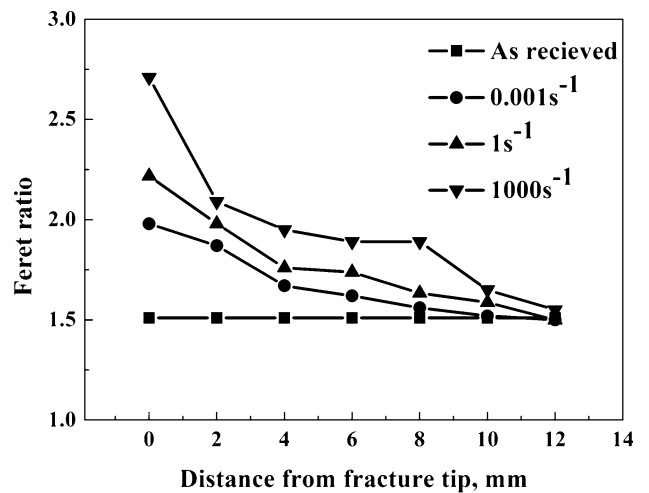


Fig. 12 Average Feret ratio as a function of distance from the fracture tip at different strain rates

Table 2 Fitting parameters for the modified Johnson-Cook model and modified Zerilli-Armstrong model

Modified JC model					
<i>A</i>	<i>B</i>	<i>n</i>	<i>C</i>	<i>R</i> ²	
506.4	1341	0.4436	0.004883	0.9693	
Modified ZA model					
<i>C</i> ₀	<i>C</i> ₁	<i>m</i>	<i>C</i> ₅	<i>n</i>	<i>R</i> ²
489.7	61.30	0.1002	1372	0.4674	0.9825

tigated steels: a modified JC model, given by Eq 1, and a modified ZA model, given by Eq 2.

$$\sigma = (A + B\varepsilon^n) \cdot (1 + C \ln(\dot{\varepsilon}/\dot{\varepsilon}_0)), \quad (\text{Eq 1})$$

$$\sigma = c_0 + c_1(\dot{\varepsilon})^m + c_5\varepsilon^n, \quad (\text{Eq 2})$$

where σ is effective stress (MPa); ε is effective plastic strain; $\dot{\varepsilon}$ is strain rate (s⁻¹); $\dot{\varepsilon}_0$ is the reference strain rate, taken as 0.001 s⁻¹ in this study; *A*, *B*, *n*, *C* of Eq 1 and *c*₀, *c*₁, *c*₅, *m*, *n* of Eq 2 are constants that vary among materials.

Multivariable nonlinear fitting was conducted by 1st Opt software, the calculated parameters, as well as the coefficients of determination (*R*²) are given in Table 2 for each model. Figure 13 shows the effective strain-stress curves calculated according to the two models plotted together the experimental points for the investigated steels. As it can be seen, the results of both models were in good agreement with the experimental data at 0.001 s⁻¹. But the modified ZA (m-ZA) model was more effective at 500 s⁻¹, and the *R*² coefficient was greater than that of the modified JC (m-JC) model, it will be explained by introducing the strain-hardening rate *k*.

Strain-hardening rate *k*, which is defined by Eq 3, can quantitatively reflect the strain hardening ability of materials, and describe the deformation characteristics in the uniform plastic deformation stage.

$$k = \frac{d\sigma}{d\varepsilon}. \quad (\text{Eq 3})$$

The strain-hardening rates at various strain rates were obtained by the effective strain-stress curves, as shown in Fig. 14. The curves can be divided into two stages. In stage I, the strain-hardening rate was high, and decreased rapidly; while in stage II, the strain-hardening rate was low, and decreased slowly. The differences in strain-hardening rate in different stages indicate that the deformation mechanism of the material changes. Moreover, the strain-hardening rate was basically consistent at the same strain of different strain rates, that is to say, *k* is independent of strain rate.

The strain-hardening rate calculated by Eq 1, 2, 3 for the m-JC model and m-ZA model is shown in Eq 4 and 5, respectively.

$$k_{\text{JC}} = nB(\varepsilon)^{n-1}(1 + C \ln(\dot{\varepsilon}/\dot{\varepsilon}_0)), \quad (\text{Eq 4})$$

$$k_{\text{ZA}} = nc_5\varepsilon^{n-1}. \quad (\text{Eq 5})$$

The *k* for the m-JC model is influenced by strain rate, but the *k* for the m-ZA model is independent of strain rate. However,

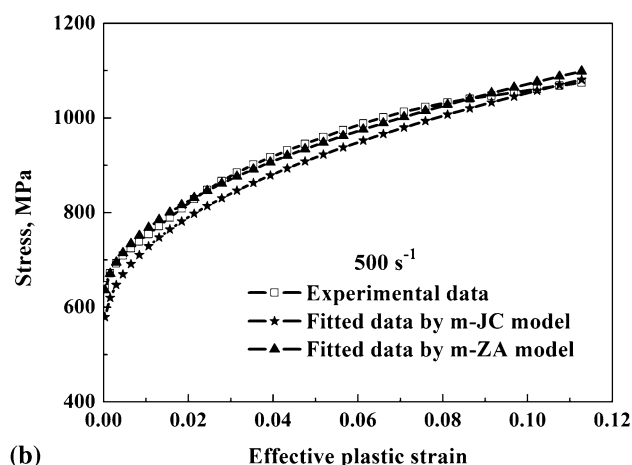
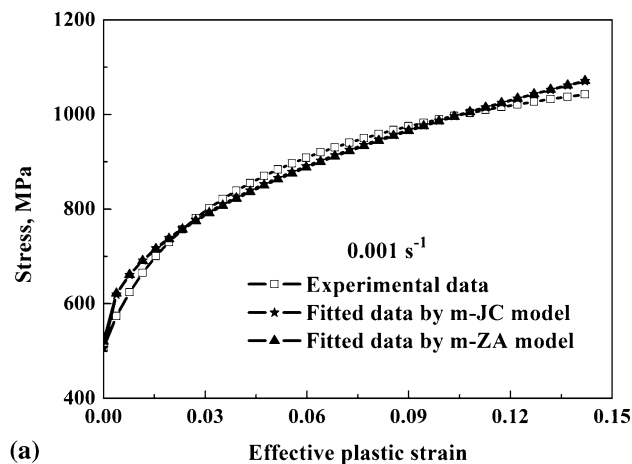


Fig. 13 Effective stress-strain curves described by the modified Johnson-Cook model and modified Zerilli-Armstrong model at (a) 0.001 s⁻¹ and (b) 500 s⁻¹

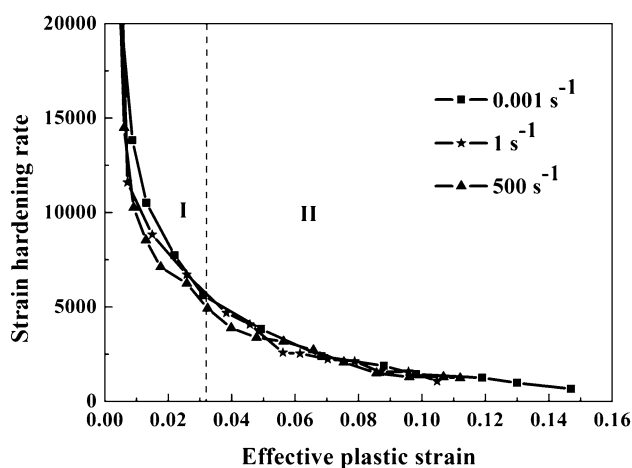


Fig. 14 Strain-hardening rates at various strain rates

the value of $C \ln(\dot{\varepsilon}/\dot{\varepsilon}_0)$ in this study is very small (range from 0 to 0.0675). Therefore, both models can effectively describe the experimental results, although the m-ZA model is more accurate.

Table 3 The dynamic factor results calculated by the modified Johnson-Cook model and modified Zerilli-Armstrong model

Strain rate, s^{-1}	1	10	100	500	1000
$\frac{DF(UTS)}{DF(YS)}$ by m-JC model	0.9307	0.9323	0.9296	0.9333	0.9301
$\frac{DF(UTS)}{DF(YS)}$ by m-ZA model	0.9034	0.8931	0.8766	0.8688	0.8608

As mentioned above, the strain rate sensitivity of dual phase steel can be evaluated by the dynamic factor (coded as DF), for the modified JC model, Eq 1, when $\varepsilon = 0$, $\sigma = YS$; when ε equals to the maximum of plastic strain (ε_{max}), $\sigma = UTS$. In this study, the strength at a strain rate of $0.001 s^{-1}$ ($\varepsilon_{max} = 0.1461$) was defined as the divisor to calculate the dynamic factors of YS and UTS. So the DF at strain rate of $\dot{\varepsilon}$ can be expressed as

$$DF(YS) = 1 + C \ln(\dot{\varepsilon}/\dot{\varepsilon}_0), \quad (\text{Eq 6})$$

$$DF(UTS) = \frac{(A + B\varepsilon_{max}^n) \cdot (1 + C \ln(\dot{\varepsilon}/\dot{\varepsilon}_0))}{A + B \cdot 0.1461^n}, \quad (\text{Eq 7})$$

$$\frac{DF(UTS)}{DF(YS)} = \frac{A + B\varepsilon_{max}^n}{A + B \cdot 0.1461^n} = \frac{506.4 + 1341\varepsilon_{max}^{0.4436}}{1077.7}. \quad (\text{Eq 8})$$

Similarly, for the modified ZA model,

$$\frac{DF(UTS)}{DF(YS)} = \frac{0.482 \cdot (489.7 + 61.3(\dot{\varepsilon})^{0.1002} + 1372\varepsilon^{0.4674})}{489.7 + 61.3(\dot{\varepsilon})^{0.1002}}. \quad (\text{Eq 9})$$

Table 3 presents the result calculated by the model at different strain rates. For all the cases, $DF(UTS)/DF(YS) < 1$, $DF(UTS) < DF(YS)$. Thus, the yield stress is more sensitive to strain rate than the UTS. We also concluded from Eq 8 that the main reason why $DF(UTS) < DF(YS)$ was the maximum of plastic strain at higher strain rate was smaller than that of lower strain rate. That is to say, $DF(UTS) < DF(YS)$ is related to the uniform elongation.

4. Conclusions

1. The plastic deformation was notably affected by strain rates; the strain rate sensitivity for yield strength is greater than that for ultimate tensile strength. The product of strength and plasticity increased dramatically at $1000 s^{-1}$, and reached the maximum value, indicating the excellent performance of the studied steel at high strain rate conditions.
2. As the strain rate increased, an increasing number of voids can be observed in the tensile fracture due to the spalling of hard martensite phase. The formation of microcracks and voids by the fracture of martensite increased with increasing strain rate; however, the formation at the ferrite/martensite interface was still the major mechanism. The martensite near the tensile fracture also deformed significantly at high strain rate due to the work-softening effect caused by the adiabatic temperature rise. The strain rate effect is not evenly distributed in the plastic deformation region.
3. The constitutive equations of the investigated DP780 steel were described by a modified Johnson-Cook model

and Zerilli-Armstrong model. Both models can effectively describe the experimental results, while the m-ZA model is more accurate as the strain-hardening rate of this model is independent of strain rate.

Acknowledgment

This work was supported by the National High Technology Research and Development Program of China (No. 2013AA031601), National “Twelfth Five-Year” Plan for Science & Technology Support Program of China (No. 2012BAF04B01) and National Natural Science Foundation of China (Project U1460101).

Reference

1. S.C. Li, Y.L. Kang, and S. Kuang, Effects of Microstructure on Fatigue Crack Growth Behavior in Cold-Rolled Dual Phase Steels, *Mater. Sci. Eng. A*, 2014, **612**, p 153–161
2. M. Itabashi and K. Kawata, Carbon Content Effect on High-Strain-Rate Tensile Properties for Carbon Steels, *Int. J. Impact. Eng.*, 2000, **24**, p 117–131
3. W. Wang, M. Li, C. He, X. Wei, D. Wang, and H. Du, Experimental Study on High Strain Rate Behavior of High Strength 600-1000 MPa Dual Phase Steels and 1200 MPa Fully Martensitic Steels, *Mater. Des.*, 2012, **47**, p 510–521
4. C.C. Roth and D. Mohr, Effect of Strain Rate on Ductile Fracture Initiation in Advanced High Strength Steel Sheets: Experiments and Modeling, *Int. J. Plast.*, 2014, **56**, p 19–44
5. S. Oliver, T.B. Jones, and G. Fourlaris, Dual Phase Versus TRIP Strip Steels: Microstructural Changes as a Consequence of Quasi-static and Dynamic Tensile Testing, *Mater. Charact.*, 2007, **58**, p 390–400
6. S. Oliver, G. Fourlaris, and T.B. Jones, Dual Phase Versus TRIP Strip Steels: A Comparison of Dynamic Properties for Automotive Crash Performance, *Mater. Sci. Technol.*, 2007, **23**, p 423–431
7. J. Huh, H. Huh, and C.S. Lee, Effect of Strain Rate on Plastic Anisotropy of Advanced High Strength Steel Sheets, *Int. J. Plast.*, 2013, **44**, p 23–46
8. D.Y. Dong, Y. Liu, L. Wang, and L.J. Su, Effect of Strain Rate on Dynamic Deformation Behavior of DP780 Steel, *Acta. Metall. Sin.*, 2013, **49**, p 159–166
9. V. Tarigopula, O.S. Hopperstad, M. Langseth, A.H. Clausen, and F. Hild, A Study of Localisation in Dual-phase High-Strength Steels under Dynamic Loading Using Digital Image Correlation and FE Analysis, *Int. J. Solids Struct.*, 2008, **45**, p 601–619
10. A. He, G.L. Xie, H.L. Zhang, and X.T. Wang, A Comparative Study on Johnson-Cook, Modified Johnson-Cook and Arrhenius-type Constitutive Models to Predict the High Temperature Flow Stress in 20CrMo Alloy Steel, *Mater. Des.*, 2013, **52**, p 677–685
11. R.B. Song and Q.F. Dai, Dynamic Deformation Behavior of Dual Phase Ferritic-Martensitic Steel at Strain Rates from 10^{-4} to $2000 s^{-1}$, *J. Iron Steel Res. Int.*, 2013, **20**, p 48–53
12. A. Nouri, H. Saghafian, and S. Kheirandish, Effects of Silicon Content and Intercritical Annealing on Manganese Partitioning in Dual Phase Steels, *J. Iron Steel Res. Int.*, 2010, **17**, p 44–50

13. J.B. Qu, W. Dabboussi, F. Hassani, J. Nemes, and S. Yue, Effect of Microstructure on the Dynamic Deformation Behavior of Dual Phase Steel, *Mater. Sci. Eng. A*, 2008, **479**, p 93–104
14. J.H. Sung, J.H. Kim, and R.H. Wagoner, A Plastic Constitutive Equation Incorporating Strain, Strain-Rate, and Temperature, *Int. J. Plast.*, 2010, **26**, p 1746–1771
15. S.L. Yan, H. Yang, H.W. Li, and G.Y. Ren, Experimental Study of Macro-Micro Dynamic Behaviors of 5A0X Aluminum Alloys in High Velocity Deformation, *Mater. Sci. Eng. A*, 2014, **598**, p 197–206
16. G.R. Johnson and W.H. Cook, Fracture Characteristics of Three Metals Subjected to Various Strains, Strain Rates, Temperatures and Pressures, *Eng. Fract. Mech.*, 1985, **21**, p 31–48
17. F.J. Zerilli and R.W. Armstrong, Dislocation-Mechanics-Based Constitutive Relations for Material Dynamics Calculations, *J. Appl. Phys.*, 1987, **61**, p 1816